The role of nonmuscle myosin 2A and 2B in the regulation of mesenchymal cell contact guidance

Alexander S. Zhovmer[a,*], Erdem D. Tabdanov[b], Houxun Miao[c], Han Wen[c], Jinqiu Chen[d], Xiaoling Luo[d], Xuefei Ma[a], Paolo P. Provenzano[b], and Robert S. Adelstein[a,*]

[a]Laboratory of Molecular Cardiology and [c]Imaging Physics Laboratory, National Heart, Lung, and Blood Institute, Bethesda, MD 20814; [b]Laboratory for Engineering in Oncology, University of Minnesota, Minneapolis, MN 55455; [d]Collaborative Protein Technology Resource, National Cancer Institute, Bethesda, MD 20892

ABSTRACT **Contact guidance refers to the ability of cells to sense the geometrical features of the microenvironment and respond by changing their shape and adopting the appropriate orientation. Inhibition and ablation of nonmuscle myosin 2 (NM2) paralogues have demonstrated their importance for contact guidance. However, the specific roles of the NM2 paralogues have not been systematically studied. In this work we use micropatterned substrates to examine the roles of NM2A and NM2B and to elucidate the relationship of the microenvironment, actomyosin, and microtubules in contact guidance. We show that contact guidance is preserved following loss of NM2B and that expression of NM2A alone is sufficient to establish an appropriate orientation of the cells. Loss of NM2B and overexpression of NM2A result in a prominent cell polarization that is found to be linked to the increased alignment of microtubules with the actomyosin scaffold. Suppression of actomyosin with blebbistatin reduces cell polarity on a flat surface, but not on a surface with contact guidance cues. This indicates that the lost microtubule–actomyosin interactions are compensated for by microtubule–microenvironment interactions, which are sufficient to establish cell polarity through contact guidance.**

Monitoring Editor
Yu-li Wang
Carnegie Mellon University

Received: Jan 31, 2019
Revised: Jun 25, 2019
Accepted: Jul 3, 2019

INTRODUCTION

The ability of cells to sense the geometrical characteristics of their microenvironment and respond by changing their shape and adopting the appropriate orientation was initially discovered in 1912 using frog and chick embryos (Harrison, 1912). It was named contact guidance in 1945 (Weiss, 1945). Over the years contact guidance was recognized as an important mechanism in embryogenesis (Hay, 2005), wound repair (Gurtner *et al.*, 2008), and cancer progression (Erdogan *et al.*, 2017; Brabletz *et al.*, 2018). Various tests demonstrated that the orientation of cells can be influenced by a gradient of adhesion sites, as well as steric and geometrical features (Weiss and Garber, 1952; Provenzano *et al.*, 2008; Jansen *et al.*, 2015). Just as cells seeded onto flat substrates generally exhibit a random orientation, cells seeded onto substrates that have microgrooves orient along the direction of these physical cues (Walboomers *et al.*, 1999; Loesberg *et al.*, 2007). A similar orientation can be achieved using flat non-adhesive substrates with printed lines of adhesive proteins where cells align along the adhesive lines (Nesmith *et al.*, 2011).

The microtubule system is known to play an important role in the navigation of the neural cone (Williamson *et al.*, 1996), three-dimensional cell motility (Bouchet and Akhmanova, 2017), and contact guidance in retinal pigment epithelium-1 cells (Lee *et al.*, 2016) and fibroblast cells (Oakley and Brunette, 1995). In MDA-MB-231 tumor cells, cell alignment through contact guidance requires predominantly microtubules. It also requires the proper balance between transverse actin arcs and dorsal/ventral stress fibers (Tabdanov *et al.*, 2018). Microtubules and actin structures engage in extensive crosstalk in the regulation of cell shape and cell polarity (for details see Dogterom and Koenderink, 2019). Results from in vitro reconstitution experiments demonstrate that microtubules interact with the cortical actin meshwork, which acts as a physical barrier impeding microtubule growth and subsequently promoting the occurrence of

This article was published online ahead of print in MBoC in Press (http://www.molbiolcell.org/cgi/doi/10.1091/mbc.E19-01-0071) on July 17, 2019.

*Address correspondence to: Alexander Zhovmer (zhovmera@nih.gov); Robert S. Adelstein (adelster@nhlbi.nih.gov).

Abbreviations used: MT, microtubule; NM2, nonmuscle myosin 2; SF, stress fiber.

microtubular catastrophes (Janson *et al.*, 2003; Colin *et al.*, 2018). It has been also shown in vitro, using the engineered microtubule/actin binding protein (TipAct), that actin bundles can act as a scaffold that guides the growing microtubule ends (Preciado Lopez *et al.*, 2014). In cell division, the actin-binding protein moesin anchors microtubules and stabilizes them at the cell cortex (Solinet *et al.*, 2013). However, the mechanisms underlying actin and microtubule interactions are still largely unknown, especially in the regulation of cell polarity in response to contact guidance.

Nonmuscle myosin 2 (NM2) plays an important role in regulating the actin cytoskeleton. The inhibition or ablation of NM2s is known to affect actomyosin organization and the migration of cells (Vicente-Manzanares *et al.*, 2009). NM2A has been shown to be involved in the regulation of interactions between microtubules and actomyosin (Even-Ram *et al.*, 2007). Moreover, actomyosin and microtubules share multiple Rho GTPase regulators, such as GEF-H1, which mediates RhoA activation to regulate three-dimensional motility in T47D human breast carcinoma cells (Heck *et al.*, 2012) or directional migration of HeLa cells (Nalbant *et al.*, 2009). It has also been suggested that NM2B has a specific role in contact guidance, as exogenous NM2A expression is unable to rescue the defects of directional stability of migration and the ability to respond to mechanical stimulation in the NM2B ablated fibroblasts (Lo *et al.*, 2004) and the defects of growth cone turning along a laminin border in the NM2B ablated growing neural cone (Turney and Bridgman, 2005). Yet the specific roles for NM2A and NM2B paralogues in contact guidance have not been studied systematically to date.

In this work we used micropatterned substrates to examine the roles of the NM2A and NM2B paralogues and elucidate the relationship of the microenvironment, actomyosin, and microtubules in the regulation of cell shape in response to contact guidance. We show that contact guidance per se is preserved following the loss of NM2B. The loss of NM2B results in a marked cell polarization established through contact guidance or spontaneously due to intrinsic factors. We link gain of polarization to increased alignment of microtubules with either the actomyosin scaffold or geometrical patterns that help to establish cell polarity through contact guidance.

RESULTS

Contact guidance is preserved following loss of NM2B

We chose a microprinting technique and a fibronectin coating for micropatterns in order to study the ability of mesenchymal cells (fibroblasts and fibroblast-like cells) to sense the geometrical characteristics of their microenvironment and respond by adopting the appropriate orientation. The microprinting technique provides a faithful biomimetic recapitulation of anisotropic architectures (substrates with different properties in different directions), while the fibronectin coating allows a highly directional persistence of migration for both fibroblasts (Missirlis *et al.*, 2016) and cancer cells (Erdogan *et al.*, 2017).

The basic platform for contact guidance was an array of microstumps, here termed "micropillars" (Figure 1A), that provided bidirectional physical cues. We also tested complementary substrates with additional combinations of physical cues and adhesion cues for a more complete comparison of cell responses through contact guidance. Microgrooves were used to provide unidirectional physical cues, while flat parallel microlines and their combination into orthogonal grids were used to supply uni- and bidirectional adhesion cues, respectively (Supplemental Figure S1A). The overall amount of actin cytoskeletal structures in a given direction, visualized by phalloidin staining, is used to analyze the preferred alignment of cells established through contact guidance (Figure 1Ba). The histograms on the right of the figure indicate the percentage of actin structures in a given direction. Images with a completely random alignment of cells are expected to give a flat (isotropic) histogram (Figure 1Bb, top), whereas images in which cells have a preferred orientation along orthogonal axes of the micropillar rows are expected to give an anisotropic histogram with a peak at that orientation (Figure 1Bb, bottom).

We studied mouse embryonic fibroblasts (wt MEF) and fibroblasts from NM2B-ablated mouse embryos (MEF 2B–/–), which show comparable levels of NM2A expression, as demonstrated by immunoblots (Supplemental Figure S1B, third row) and capillary-based immunoassays (Supplemental Figure S1C). The MEF 2B–/– cells express neither NM2B nor NM2C (Supplemental Figure S1, B, first and fifth rows, C, and D). In addition to the MEF cells, we tested the fibroblast-like COS-7 cell line, since it lacks NM2A expression, and expresses primarily NM2B with only small amounts of NM2C (Bao *et al.*, 2005). The spread cell morphology of each cell line was examined using micropatterns and characterized relative to the expression of NM2A and NM2B.

On micropillars, both wt MEF and MEF 2B–/– cells display a directional response (Figure 1C, a and b, zoomed-in views below, e and f). The preferred directional orientation of the cells was analyzed using the directionality plugin (FIJI) following F-actin staining. Panels 1Ci and 1Cj are histograms showing the distribution of cell alignment along the bidirectional cues. Notably, wt MEF cells developed protrusions oriented along both axes of the micropillar rows, acquiring a strongly biaxial cell shape (Figure 1Ca). In contrast, MEF 2B–/– cells developed a predominantly polarized uniaxial cell shape, sporadically aligning a spindle-shaped body to either of two axes along the micropillar rows (Figure 1Cb). The COS-7 cells, which lack NM2A, demonstrated a negligible directional orientation along the micropillar cues (Figure 1C, c, g, and k). Of note, introduction of exogenous NM2A into COS-7 cells results in a directional response to micropillar cues (Figure 1C, d, h, and l). These results, summarized in Table 1, show that contact guidance is preserved following loss of NM2B, since expression of NM2A alone is sufficient to establish an appropriate cell orientation. The loss of NM2B results in prominent cell polarization on micropillars. The presence of NM2A ensures cell polarization established through contact guidance.

On complementary substrates, wt MEF and MEF 2B–/– cells also display a directional response either to the microline (Figure 2, a and b), grid (Figure 2, d and e), or microgroove cues (Figure 2, g and h), whereas the COS-7 cells have a negligible directional orientation along all these three cues (microlines, Figure 2c; grids, Figure 2f; and microgrooves, Figure 2i). Notably, the grids induced a directional response across wt MEF and MEF 2B–/– cells (Figure 2, d and e; Supplemental Movies 1 and 2) identical to the ones induced by the micropillars, where wt MEF cells developed a biaxial cell shape and MEF 2B–/– cells developed a predominantly uniaxial cell shape.

Distinct functions of NM2A and NM2B in the regulation of cell polarization

Geometrical cues from the microenvironment are known to affect cell shape (Mogilner and Keren, 2009). As shown above, the loss of NM2B increases the polarization of MEF cells acquired through contact guidance on micropillars and grids. To separate out the role of NM2 paralogues from the role of geometrical cues, we used a 2D flat surface, where the external geometrical cues are absent, and fibroblasts routinely acquire a predominantly multiaxial (nonpolarized) cell shape (Doyle *et al.*, 2009; Hung *et al.*, 2016). Notably,

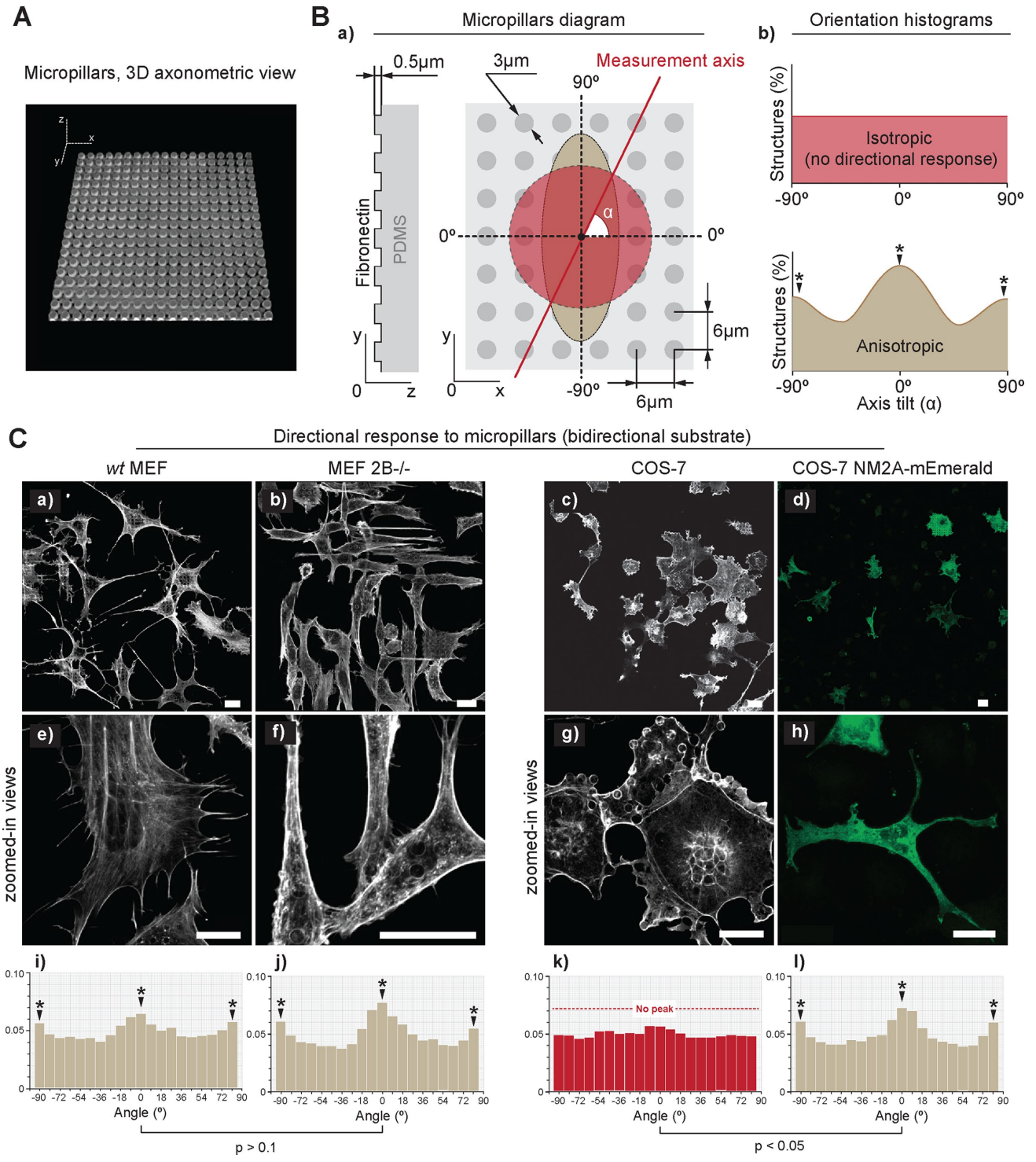

FIGURE 1: Contact guidance is preserved upon the loss of NM2B in mesenchymal cells. (A) Picture of the fibronectin–Alexa-555 coated micropillars that serve as a bidirectional substrate with physical cues. (B) Diagram showing the method used to analyze the preferred orientation of structures present in the input image. Images with no preferred orientation (a, red circle) are expected to give a flat histogram (b, Top), whereas images with a preferred orientation (a, beige oval) are expected to give a histogram with a peak at the specific angle (b, Bottom, arrowheads with asterisks). (C) Confocal images of wt MEF (a, e), MEF 2B–/– (b, f), and COS-7 cells (c, g) stained for F-actin (phalloidin), and COS-7 cells exogenously expressing NM2A-mEmerald (d, h;. mEmerald fluorescence) cultured on micropillars show that wt MEF cells adapt a biaxial shape (a, enlarged in e) and MEF 2B–/– cells acquire an uniaxial shape (b, enlarged in f). COS-7 cells show no directional orientation (c, enlarged in g). Exogenous expression of NM2A-mEmerald in COS-7 cells results in an increased directional orientation of COS-7 cells (d, enlarged in h; $n \geq 25$ cells, from ≥3 different fields of view). Panels i–l are histograms showing quantification of preferred cell orientation for each type of cell that was analyzed. All p values are for the two-sample Kolmogorov–Smirnov test. Scale bars are 25 µm.

	wt MEF	MEF 2B–/–	COS-7	COS-7 NM2A-mEmerald
NM2 expression:	NM2A + NM2B	NM2A	NM2B	NM2A + NM2B
Directional response:	Anisotropic	Anisotropic	Isotropic	Anisotropic
Cell morphology:	Biaxial	Uniaxial	Polygonal	Biaxial

Contact guidance is preserved following loss of NM2B. Expression of NM2A alone is sufficient for contact guidance. The loss of NM2B results in prominent cell polarization on micropillars.

TABLE 1: Directional response to the micropillar cues.

unlike wt MEF cells, MEF 2B–/– cells maintain a polarized cell shape on a 2D surface. Namely, wt MEF cells develop multiple (4 ± 1.4) protrusions per cell (Figure 3A, a and c; Supplemental Movie 3). In contrast, MEF 2B–/– cells develop (2.4 ± 0.8) protrusions per cell (Figure 3A, b and c; Supplemental Movie 4). Thus the loss of NM2B leads to spontaneous polarization of MEF 2B–/– cells on a 2D flat surface.

The increased polarization of MEF 2B–/– cells coincides with an increased migration velocity (15.7 ± 13.5 μm/h) compared with that of wt MEF cells (11.2 ± 8.2 μm/h; Supplemental Figure S2), along with a lack of mature focal adhesions (Supplemental Figure S3), as was previously reported (Lo *et al.*, 2004). Stress fibers in nonmotile cells are relatively stable. In contrast, highly motile cells typically contain more dynamic stress fibers (Pellegrin and Mellor, 2007). We hypothesize that the dynamics of the actomyosin structure increases in MEF 2B–/– cells. To test this hypothesis, we analyzed NM2A fluorescence recovery after photobleaching (FRAP) in wt MEF (Supplemental Figure S4Aa) and MEF 2B–/– (Supplemental Figure S4Ab) cells. The FRAP analysis indicated that NM2A dynamics was markedly increased in MEF 2B–/– cells from that in wt MEF cells, as indicated by significantly faster recovery of the signal following photobleaching (Supplemental Figure S4B, T-half). We also found that loss of NM2B resulted in a decrease in the NM2A mobile fraction in MEF 2B–/– cells compared with that in wt MEF cells. This may partially reflect a compensatory effect of NM2A function due to the loss of NM2B.

The actomyosin dynamics affects the overall architecture of stress fibers, since de novo stress fiber formation occurs by slow coalescence of smaller bundles (Shutova *et al.*, 2017). Because the actomyosin dynamics was increased following loss of NM2B, we expect to find more stress fibers in MEF 2B–/– cells. To estimate the changes in actomyosin structure following loss of NM2B, we used the ratio of the actomyosin projection area to the cell projection area. This ratio indicates that actomyosin structures occupy 29 ± 9% of the cell projection area in wt MEF cells (Figure 3B, a and e) compared with 51 ± 11% in MEF 2B–/– cells (Figure 3B, b and e). Alternatively, calculated by phalloidin-stained F-actin, the actomyosin structures occupy 31 ± 8% of the cell projection area in wt MEF cells (Figure 3B, c and f) and 55 ± 11% in MEF 2B–/– cells (Figure 3B, d and f). Cell flattening, an indicator of the actomyosin accumulation (Burnette *et al.*, 2014; Vishavkarma *et al.*, 2014; Li *et al.*, 2015), was also observed in MEF 2B–/– cells down to 8 ± 1 μm from 10 ± 2 μm for wt MEF cells (Supplemental Figure S5). Of note, the introduction of exogenous NM2A but not NM2B into COS-7 cells results in a prominent accumulation of actomyosin structures (Supplemental Figure S6, top panel shows NM2 immunofluorescence, middle panel shows phalloidin staining, bottom panel shows quantification), as was reported previously (Shutova *et al.*, 2017).

To further illustrate the role of NM2 paralogue in cell polarization, we expressed exogenous NM2A and NM2B in MEF 2B–/– and COS-7 cells. The resultant cell shapes were analyzed using the aspect ratio of a fitted ellipse, where the aspect ratio is the ratio of the major cell axis to the minor cell axis. An increase in the aspect ratio indicates a greater degree of cell polarization. The baseline aspect ratio of MEF 2B–/– cells is 4.2 ± 3.5 (Figure 3C, a and g). Introduction of NM2B-mEmerald decreases their aspect ratio to 2 ± 0.7 (Figure 3C, b and g). That resembles the 1.9 ± 0.9 aspect ratio of wt MEF cells (image not shown; Figure 3Cg). Introduction of NM2A-mEmerald does not affect the aspect ratio of MEF 2B–/– cells (3.9±2.4; Figure 3C, c and g). Notably, introduction of NM2A-mEmerald increases the baseline aspect ratio of COS-7 cells from 1.3 ± 0.2 to 2.9 ± 1.3 (Figure 3C, d, f, and g). Introduction of NM2B-mEmerald does not affect the aspect ratio of 1.3 ± 0.5 of the COS-7 cells (Figure 3C, e and g).

These results indicate that the resultant cell polarization is not solely dictated by geometrical cues from the microenvironment that is extrinsically defined bi- or unidirectionality of the microenvironment. It is also predetermined by an intrinsic cell-based NM2-dependent mechanism. NM2A functions to establish and maintain cell polarity while NM2B breaks cell polarity. The presence of NM2A alone secures cell polarization either along the contact guidance cues or in a random orientation in the absence of these cues, whereas the presence of NM2B decreases cell polarization, enabling multiaxial morphology and alignment through contact guidance.

Microtubules are guided by the intracellular geometry of actomyosin

To elucidate the relationship of the microenvironment and actomyosin with respect to contact guidance we used blebbistatin (50 μM, 6 h). Inhibition of actomyosin by blebbistatin prevents the spontaneous polarization of MEF 2B–/– cells on a 2D flat surface (Supplemental Figure S7A). In contrast, blebbistatin treatment, as well as treatment with the RhoA inhibitor Y-23732 (10 μM, 6 h), does not alter the cell shape, which is biaxial for wt MEFs and is uniaxial for MEF 2B–/– cells on the micropillars (Supplemental Figure S7B). This indicates that the cell polarization and orientation acquired through contact guidance are not solely due to actomyosin.

The microtubule system is known to play an important role in cell polarization (Vasiliev *et al.*, 1970; Pegtel *et al.*, 2007; Tortosa *et al.*, 2017). To estimate the contribution of microtubules to contact guidance, we used nocodazole (2 μg/ml, 6 h), which depolymerizes microtubules. Nocodazole treatment abolishes cell polarization on a 2D flat surface (Supplemental Figure S8A). Moreover, unlike blebbistatin or Y-23732, nocodazole also abolishes cell polarization and directional orientation on micropillars (Supplemental Figure S8B). Notably, the effect of nocodazole is reversible. Contact guidance is restored and the cells recover their characteristic shapes (multiaxial for wt MEF and uniaxial for MEF 2B–/– cells) after the regrowth of microtubules following nocodazole washout (Supplemental Figure S8C). These experiments indicate that the regulation of cell shape is linked to the cooperation of the microenvironment with both actomyosin and microtubules. The microtubule network is sufficient to establish cell polarization through contact guidance where the lost

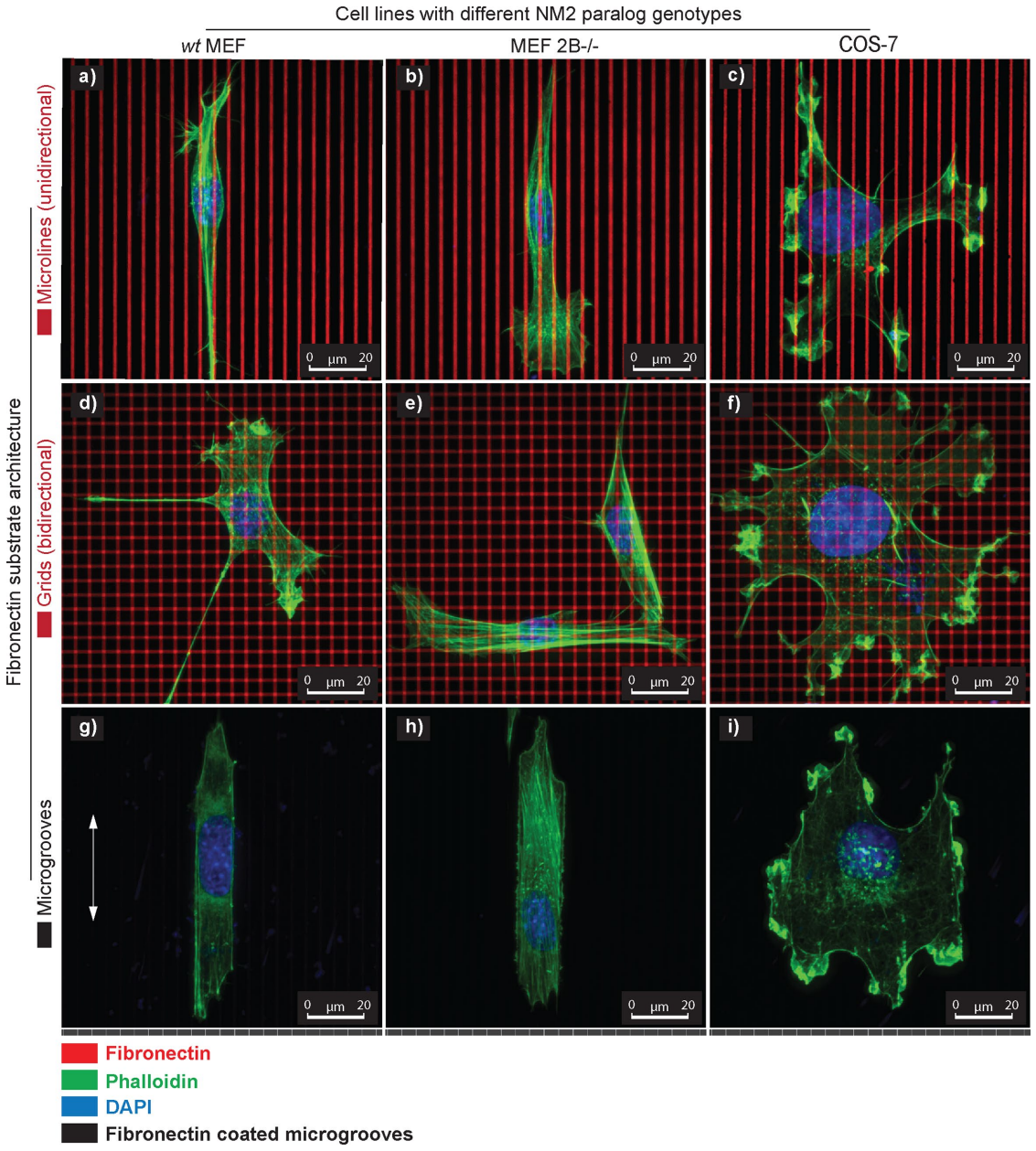

FIGURE 2: Directional orientation upon the loss of NM2B on microlines, grids, and microgrooves. iSIM (instant structural illumination microscopy) images stained for F-actin (phalloidin, green), nuclei (DAPI, blue), and fibronectin (red). (a–c) Cell orientation on fibronectin microlines. wt MEF (a) and MEF 2B–/– cells (b) acquire an overall uniaxial cell shape. COS-7 cells (c) display a polygonal cell shape. (d–f) Cell orientation on fibronectin grids. wt MEF cells (d) develop a biaxial cell shape, while MEF 2B–/– cells (e) acquire an uniaxial cell shape irrespective of bidirectionality of the underlying substrate. COS-7 cells (f) develop a polygonal cell shape. (g–i) Cell orientation on microgrooves. wt MEF (g) and MEF 2B–/– cells (h) acquire an overall uniaxial cell shape, while COS-7 cells (i) display a polygonal cell shape and are unable to follow the geometry of the pattern. Note that the fibronectin is coated over the microgrooves but not stained. Scale bars are 20 µm.

microtubule–actomyosin interactions can be compensated for by microtubule–substrate interactions, whereas both actomyosin and microtubules are needed to secure cell polarization on a flat surface.

It has been recognized that not only can extrinsic cues induce cell polarity, but also cell-intrinsic cues generated from the microtubule system can induce and maintain polarity (Siegrist and Doe, 2007). We next asked whether and how the microtubule and actomyosin cytoskeletons cooperate in response to contact guidance. We examined the microtubule organization in wt MEF (Figure 4, Aa and Ba), MEF 2B–/– (Figure 4, Ab and Bb), and COS-7 (Figure 4, Ac and Bc) cells, by analyzing the subcellular microtubule alignment at the cell–surface interface (Figure 4Ca). The percentage of microtubules aligned with a predominant collective axis was higher in MEF 2B–/– cells (51 ± 24%) than in wt MEF (46 ± 24%) or COS-7 cells (47 ± 23%) (Figure 4Cb). We further analyzed the coalignment between the actin filaments and microtubule systems (Figure 5) using angular divergence between the dominant directions of actin filaments and

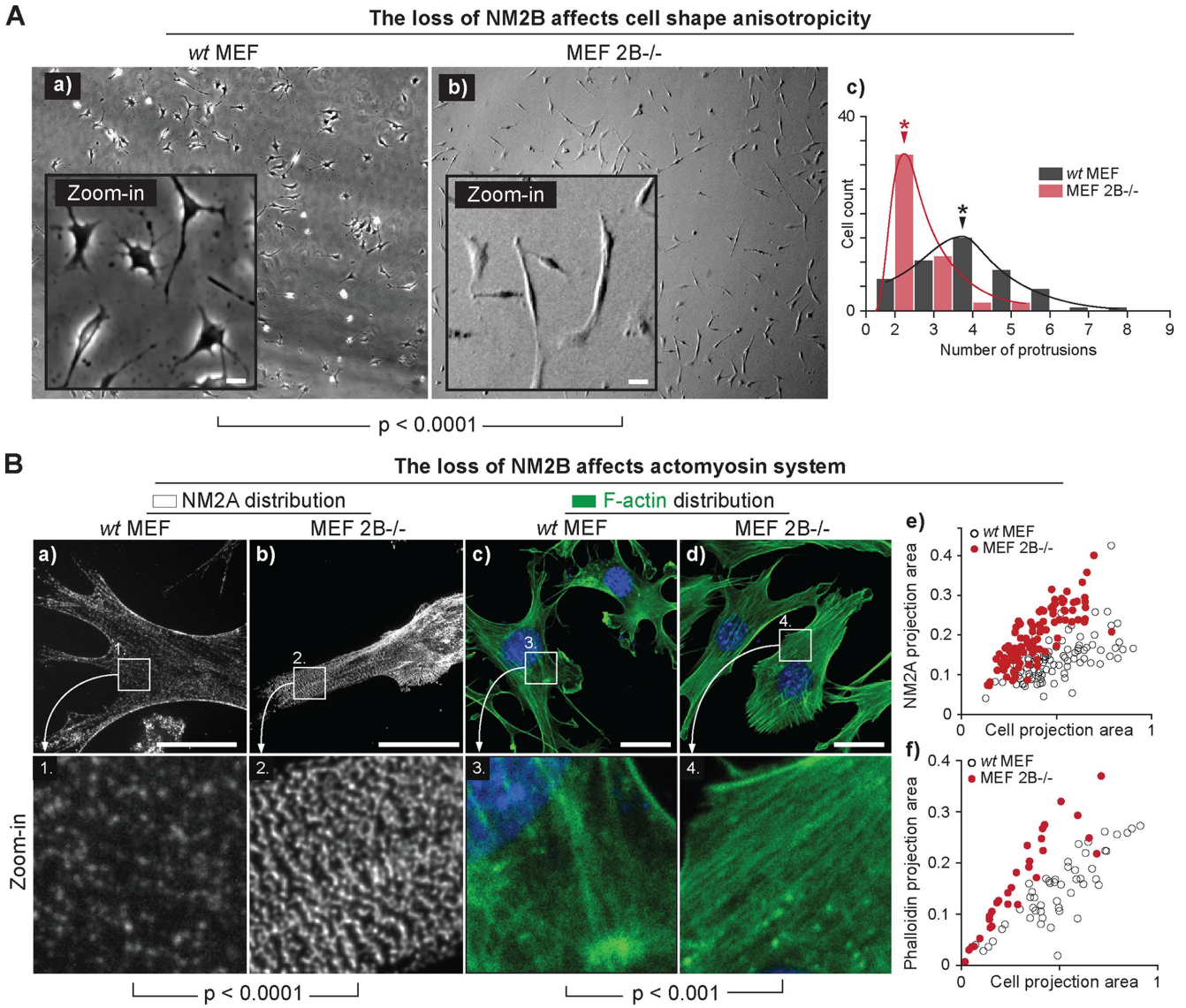
A
The loss of NM2B affects cell shape anisotropicity
wt MEF
MEF 2B-/-
a)
b)
Zoom-in
Zoom-in
c)
40
0
Cell count
*
*
wt MEF
MEF 2B-/-
0 2 3 4 5 6 7 8 9
Number of protrusions
p < 0.0001
B
The loss of NM2B affects actomyosin system
NM2A distribution
F-actin distribution
wt MEF
MEF 2B-/-
wt MEF
MEF 2B-/-
a)
b)
c)
d)
1.
2.
3.
4.
Zoom-in
1.
2.
3.
4.
p < 0.0001
p < 0.001
e)
wt MEF
MEF 2B-/-
NM2A projection area
0.4
0.3
0.2
0.1
0
0
Cell projection area
1
f)
wt MEF
MEF 2B-/-
Phalloidin projection area
0.4
0.3
0.2
0.1
0
0
Cell projection area
1
C
Cell shape anisotropicity changes after NM2 transfection
Non-transfected
Plasmid NM2B-mE
Plasmid NM2A-mE
MEF 2B-/-
COS-7
a)
b)
c)
d)
e)
f)
g)
p > 0.6
p < 0.0001
p < 0.001
p < 0.005
p < 0.0001
p > 0.5
Aspect ratio (length/width)
0
2
4
6
8
MEF 2B-/-
MEF
COS-7
+NM2A mE
+NM2B mE
2B-/-
wt
+NM2A mE
+NM2B mE
wt

microtubules as an indicator of coalignment (0° indicates parallel, 90° indicates orthogonal). In MEF 2B–/– cells, the coalignment between microtubules (Figure 5d) and actin filaments (Figure 5e) is increased both in the peripheral (7° ± 6°) and in the central (12° ± 12°) areas (Figure 5f), compared with the peripheral (10° ± 13°) and central (26° ± 23°) areas of wt MEF cells, respectively (Figure 5, a–c). The COS-7 cells, which lack NM2A and thus any significant actomyosin architecture, display a general loss of coalignment between the residual actin filaments and microtubules both in the peripheral (28° ± 25°) and in the central (31° ± 23°) areas (Figure 5, g–i). Figure 5j illustrates the measurement of angular divergence.

To understand the relationship of the actomyosin and microtubule systems with respect to cell polarization, we visualized the interactions between microtubules and actomyosin using the microtubule (+)end tracking protein CLIP170-mEmerald to track microtubule growth and LifeAct-mOrange2 to visualize stress fibers in COS-7 cells, which exogenously expressed NM2A-BFP2 to increase the density of actomyosin. CLIP170 tracking indicates that the growing microtubules encounter stress fiber arrays located at the cell–surface interface and comply with their geometry (Figure 6A; Supplemental Movie 5). If the cell has low actomyosin occupancy, only a minor fraction of microtubules is guided by the actomyosin geometry and microtubules interact with actin predominantly at the cell border (Figure 6B, top panel; Supplemental Movie 6). Conversely, with the increase in actomyosin occupancy, the fraction of microtubules that encounter and follow the direction of stress fibers increases (Figure 6C; Supplemental Movie 7). Analysis of the colocalization of CLIP170 trajectories and actin structures (Figure 6D) and analysis of angular divergence between CLIP170 trajectories and actin filaments (Figure 6E) indicate that the actomyosin serves, in a dose-dependent manner, as an intracellular scaffold that directs microtubule growth.

DISCUSSION

Experiments with micropatterned substrates allowed us to separate the ability of cells to establish an appropriate orientation from cell polarization. We show that contact guidance is preserved following loss of NM2B in MEF cells and that expression of NM2A alone is sufficient to establish an appropriate cell orientation. However, loss of NM2B and overexpression of NM2A result in prominent cell polarization established either through contact guidance or spontaneously due to intrinsic factors. Furthermore, our results from the blebbistatin and nocodazole experiments with MEF cells suggest that actomyosin was not the only factor that determined cell polarity. Actomyosin cooperation with the microtubules is also required. Our experiments with live imaging in COS-7 cells (Figure 6) emphasize the physical aspect of microtubule–actomyosin cooperation for establishing cell polarization.

In epithelial cells, the inhibition of actomyosin, either by specific treatment with siRNA against NM2A or by blebbistatin, destabilizes apical–basal polarization (Lomakin *et al.*, 2015). In neural cells, NM2A contractility stabilizes the actin cytoskeleton and promotes axon growth, whereas NM2B contractility drives axon retraction (Brown *et al.*, 2009). In line with these reports, we show that in mesenchymal cells the loss of NM2B and overexpression of NM2A increase mesenchymal front–back polarity, whereas inhibition of myosin by blebbistatin and overexpression of NM2B decrease it. Together, these results indicate that NM2A has a distinct role in supporting cell polarity in mesenchymal, epithelial, and neuronal cells.

Unlike NM2A, which establishes and maintains cell polarity, NM2B appears to play a role in disassembling cell polarity. Differences in enzymatic kinetics and regulation of NM2 paralogues may contribute to their specific roles in regulating cell polarity. The increased duty ratio, compared with that for NM2A, makes NM2B particularly well suited to exert tension on actin filaments for longer periods of time (Kovács *et al.*, 2003, 2007; Wang *et al.*, 2003). In COS-7 cells, exogenous expression of NM2A increases the dynamics of stress fibers (Shutova *et al.*, 2017). In line with these reports, our data indicate that NM2A actomyosin dynamics and the overall amount of NM2A-containing actomyosin structures are increased following loss of the NM2B paralogue. Thus it appears that a dynamic actomyosin cytoskeleton containing NM2A favors cell polarization, while a stable cytoskeleton containing NM2B promotes a nonpolarized cell shape.

Normally, the NM2A and NM2B paralogues coassemble into heterotypic filaments (Beach *et al.*, 2014) of various combinations depending on cell- and tissue-specific alternative splicing of their heavy-chain genes (Li *et al.*, 2008; Jana *et al.*, 2009). In addition, it depends on the assembly state and dynamics, controlled by cell- and cell cycle–specific sets of auxiliary proteins (Schiffhauer *et al.*, 2016, 2019). Consequently, the assembly state and connectivity separate various specialized stress fiber subpopulations for each

FIGURE 3: NM2 paralogues regulate degree of cell polarization. (A) Phase-contrast images of MEF cells on a fibronectin-coated flat 2D surface show that wt MEF cells acquire a typical nonpolarized shape (a), whereas MEF 2B–/– cells display spontaneous polarization (b). wt MEF and MEF 2B–/– cells display (4 ± 1.4) and (2.4 ± 0.8) cell protrusions per cell, respectively (c; $n = 50$ cells for each cell type). Arrowheads with asterisks indicate the peaks. (B) iSIM images of MEF cells stained for NM2A (a ,b) and confocal images stained for F-actin (c, d; green, phalloidin) show increased actomyosin occupancy in MEF 2B–/– cells (b, d) compared with wt MEF cells (a,c). Panels e and f quantify the actomyosin occupancy of NM2A and F-actin, respectively. NM2A actomyosin occupies 29 ± 9% ($n = 94$ cells) of the cell projection area in wt MEF cells and 51 ± 11% ($n = 102$ cells) in MEF 2B–/– cells (e). Similarly, F-actin occupies 31 ± 8% ($n = 49$ cells) of the cell projection area in wt MEF cells and 55 ± 11% ($n = 48$ cells) in MEF 2B–/– cells (f). (C) iSIM images of MEF 2B–/– cells (a–c) stained for NM2A (a), exogenously expressing NM2B-mEmerald (b) or NM2A-mEmerald (c), and COS-7 cells (d–f) stained for NM2B (d), expressing NM2B-mEmerald (e) or NM2A-mEmerald (f). Introduction of NM2B (b) but not NM2A (c) in MEF 2B–/– cells resulted in a marked change in the cell polarity from nontransfected MEF 2B–/– cells (a). In COS-7 cells, expression of NM2A (f), but not NM2B (e), alters the original COS-7 cell shape (d). Panel (g) quantifies the cell aspect ratio from these experiments. The cell aspect ratios for wt MEF, MEF 2B–/–, NM2B-mEmerald MEF 2B–/–, and NM2A-mEmerald MEF 2B–/– cells are 1.9 ± 0.9 ($n = 34$), 4.2 ± 3.5 ($n = 37$), 2 ± 0.7 ($n = 28$), and 3.9 ± 2.4 ($n = 34$), respectively. The cell aspect ratios for COS-7 cells, NM2B-mEmerald COS-7, and NM2A-mEmerald COS-7 cells are 1.3 ± 0.2 ($n = 26$), 1.3 ± 0.5 ($n = 24$), and 2.9 ± 1.3 ($n = 36$), respectively. The cell aspect ratio of MEF 2B –/– cells is markedly decreased following the expression of NM2B. In contrast, the cells aspect ratio of COS-7 cells is significantly increased following NM2A expression. All p values are for two-sample unequal variance two-tailed t tests. Scale bars are 25 μm.

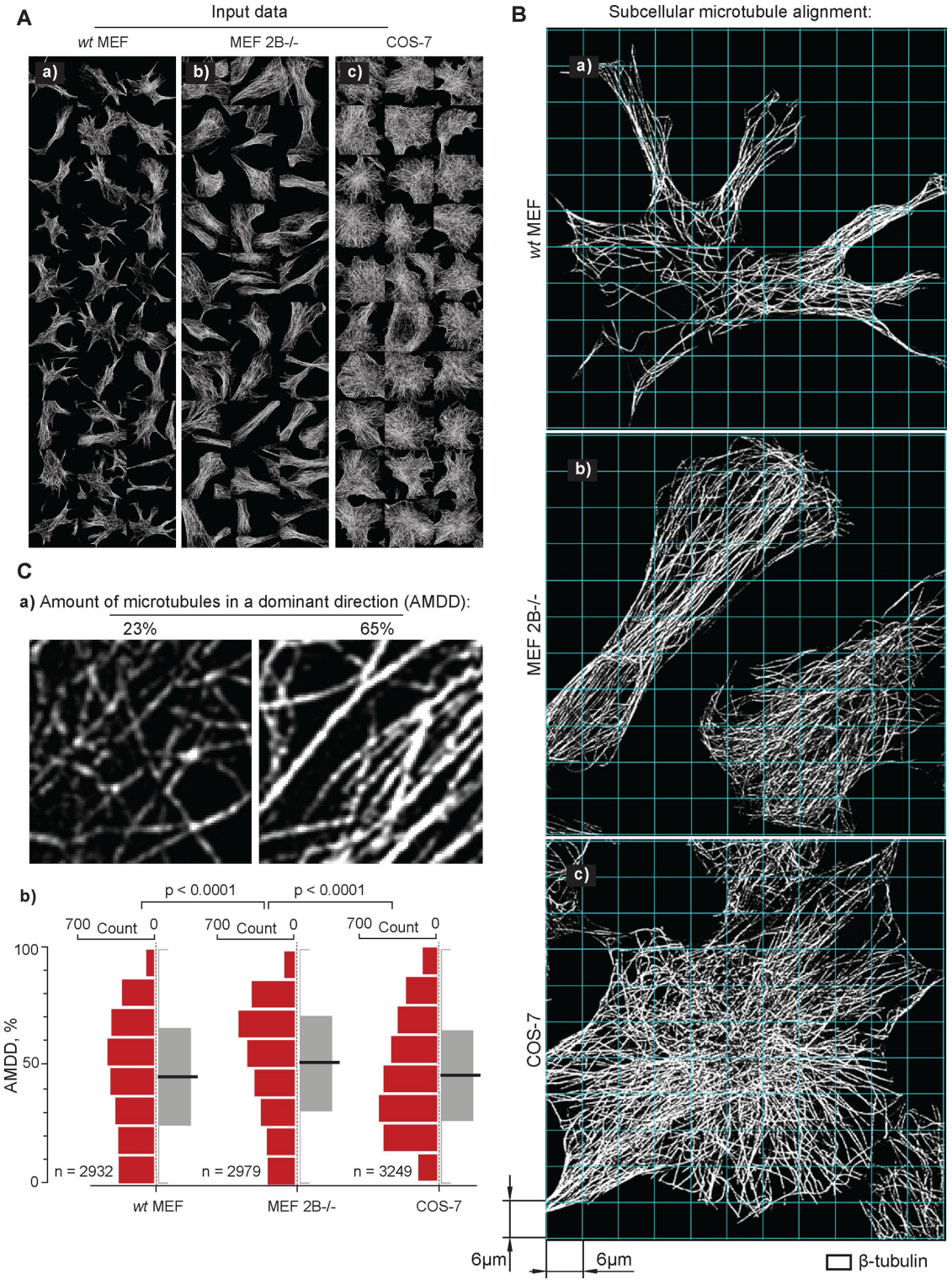

FIGURE 4: The loss of NM2B increases microtubular alignment at the cell–surface interface. (A) A collection of iSIM images of wt MEF (a), MEF 2B–/– (b), and COS-7 cells (c) stained for α-tubulin to analyze the microtubule alignment. Thirty images from each cell line are displayed. (B) Strategy of analyzing subcellular microtubule alignment. Each cell was divided by orthogonal grid (green) into individual 6 µm × 6 µm quadrants. These quadrants were then used for subcellular analysis of microtubule alignment for wt MEF (a), MEF 2B–/– (b), and COS-7 (c) cells. (C) (a) Examples of quadrants show 23% of microtubules (Left) or 65% of microtubules (Right) aligned in a dominant direction. (b) Distribution (horizontal bar, red) and average (vertical bar, gray) of the number of microtubules in a dominant direction (AMDD, %). In wt MEF cells (46 ± 24%) and COS-7 cells (47 ± 23%), microtubules are less coaligned in a dominant direction than in MEF 2B–/– cells (51 ± 24%). Data are means ± standard deviation values. All *p* values are for two-sample unequal variance two-tailed *t* tests.

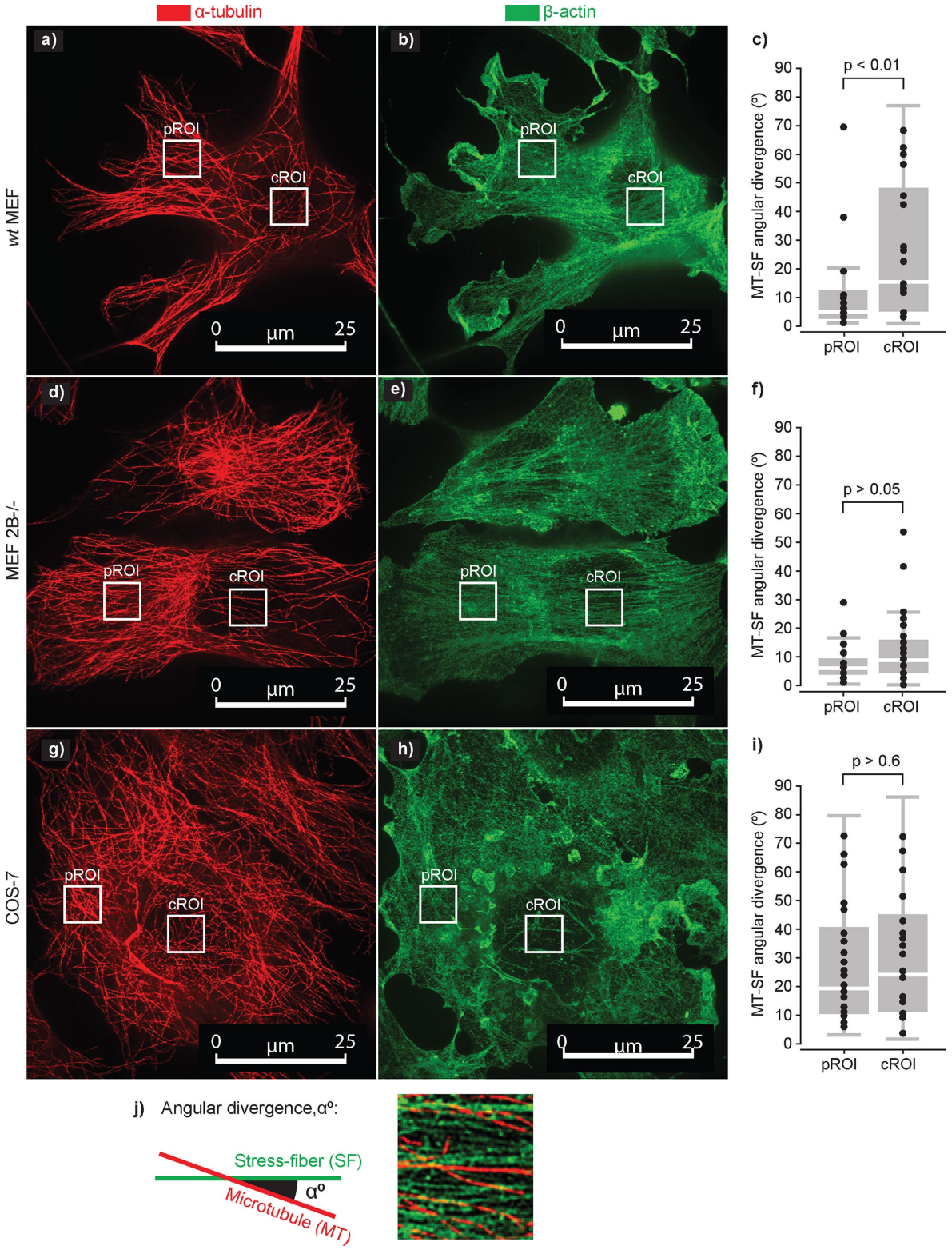

FIGURE 5: The loss of NM2B increases the coalignment of actomyosin and microtubules at the cell–surface interface. iSIM images show cells stained with antibodies for α-tubulin (a, red) and β-actin (b, green). In wt MEF cells, coalignment between microtubules (a) and actomyosin (b) is high only in peripheral regions (c). In MEF 2B–/– cells, coalignment between microtubules (d) and actomyosin (e) is high in both peripheral and central regions (f) compared with wt MEF. In COS-7 cells, coalignment between microtubules (g) and actomyosin (h) is low in both peripheral and central regions (i). Thirty cells were analyzed for each cell line. All *p* values are for two-sample unequal variance two-tailed *t* tests. Scale bars are 25 µm. (j) Angular divergence between the dominant directions of actin filaments and microtubules (indicator of coalignment, 0—parallel, 90—orthogonal) was measured in the peripheral (pROI) and central (cROI) cell regions of interest.

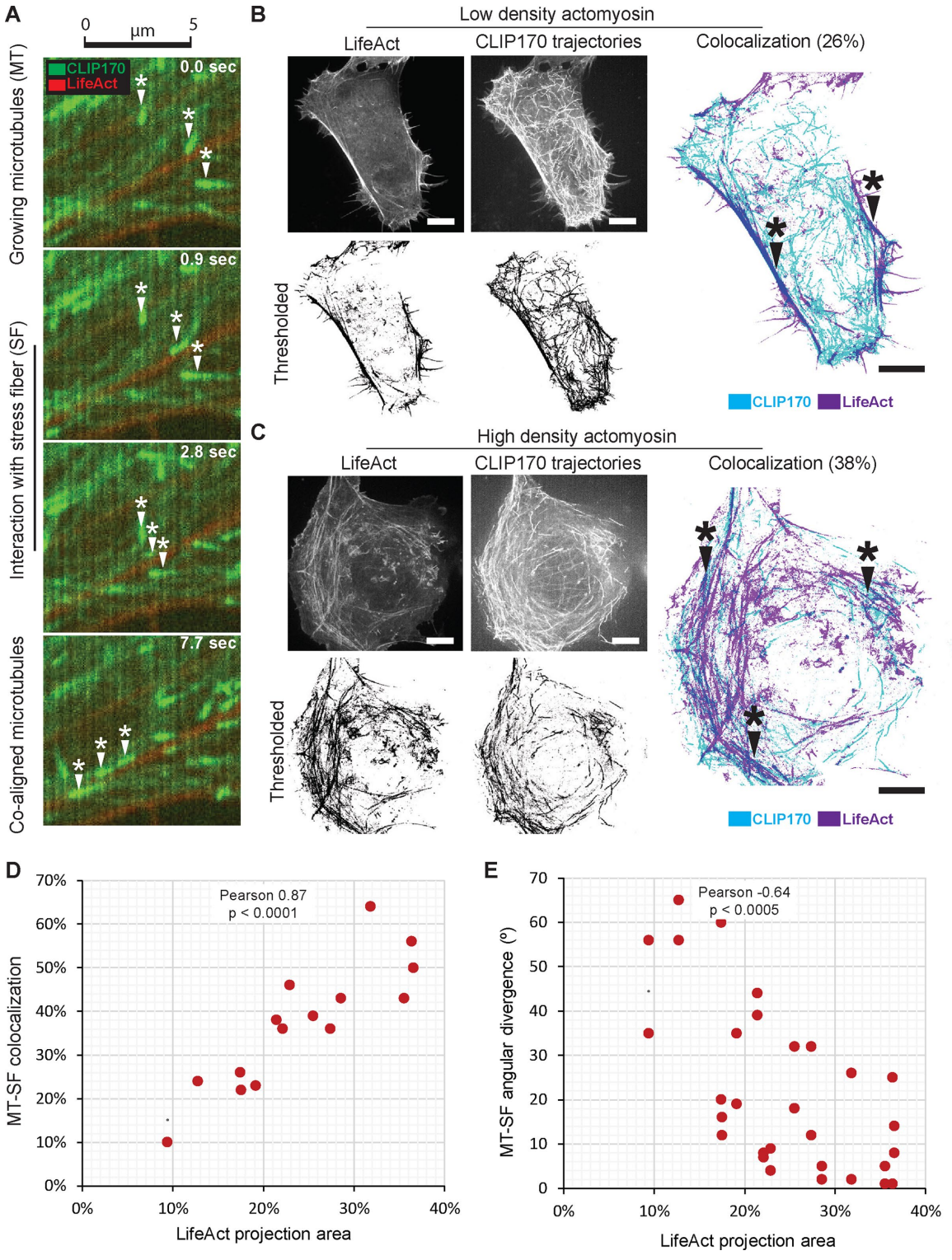

FIGURE 6: Growing microtubules use stress fibers at the cell–surface interface as a scaffold. iSIM dual-channel live imaging shows CLIP170 (green) and LifeAct (red). Simultaneous triple transfection of COS-7 cells (15 cells) with CLIP170-mEmerald (green), LifeAct-mOrange2 (red), and NM2A-BFP2 (unpublished data, used to increase actomyosin density) was imaged. (A) Three (+)ends of microtubules (arrowheads with asterisks), show dynamic interactions between the stress fiber (red, appears immobile at given acquisition rate) and growing microtubules (green) that encounter and align to a stress fiber (Supplemental Movie 5). (B) In a cell with low actomyosin occupancy, microtubules interact with actin filaments predominantly at the cell border (Supplemental Movie 6). (C) In a cell with increased actomyosin occupancy, microtubules interact with actin filaments within the entire cell (Supplemental Movie 7). (D) Actomyosin occupancy correlates positively with increased colocalization of stress fibers and microtubules (CLIP170 trajectories). (E) Actomyosin occupancy correlates negatively with angular divergence between the dominant directions of stress fibers (2 measurements for each cell) and microtubules (0—parallel, 90—orthogonal). All *p* values are for Pearson statistics. Scale bars are 25 μm.

particular cell type (Kassianidou and Kumar, 2015). Moreover, the NM2 motor activity within the central stress fibers was shown to be mediated by ROCK, whereas in the peripheral stress fibers it is regulated by MLCK (Sandquist *et al.*, 2006; Kassianidou *et al.*, 2017). In contrast, NM2B was reported to cooperate with RhoA at the rear of epithelial cells (Vassilev *et al.*, 2017). However, in neural cells, NM2B is not regulated by RhoA, whereas the NM2A pool in the central actin arcs is so regulated (Suter and Miller, 2011). These results further emphasize the unique aspects of the two myosin paralogues.

Therefore, a possible scenario is that, once the NM2A and NM2B paralogues coassemble into heterotypic filaments, the increased mechanosensitivity of NM2B (Schiffhauer *et al.*, 2016, 2019) would facilitate and reinforce NM2B enrichment in stable stress fibers that are under tension, which enhance the focal adhesions and maturation of the actomyosin cytoskeleton. Just as the actomyosin cytoskeleton plays an important role in focal adhesion formation and maturation, increased actomyosin dynamics in MEF 2B–/– cells could contribute to the decreased maturation of the focal adhesions observed in this study. Therefore, the loss of NM2B would result in thin stress fibers which are more numerous and more dynamic. These stress fibers form tightly packed arrays at the cell–surface interface due to the formation of a large number of small immature focal adhesions at the leading edge of the MEF 2B–/– cells that are seen in our study. This is consistent with the report showing that extracellular matrix geometry and initial cell adhesion strongly determine cell spreading and that cells encode a memory of their spreading history through stress fiber network organization (Kassianidou *et al.*, 2019). Consequently, we propose that microtubules induce and maintain cell polarity by their structural adaptation either to the external cues of the microenvironment or to the intracellular cues of the geometry of actomyosin cytoskeleton at the cell–surface interface.

MATERIALS AND METHODS

Substrate preparation

Micropillars (Figure 1, A and B), microgrooves (4 µm wide × 0.5 µm deep, pitch 5 µm), microlines (1 µm wide, pitch 5 µm), and orthogonal grids (1 µm wide, pitch 5 µm; Supplemental Figure S1A) were coated and printed using fibronectin (FN; ab92784, Abcam). Polydimethylsiloxane (PDMS) stamps were made by soft lithography. A silicon mold was coated with a mixture of PDMS prepolymer and the curing agent (10: 1 [w/w], Sylgard 184 silicone elastomer kit, Dow Corning) and cured for 4 h at 65°C in a convection oven. The cured PDMS was gently removed and cut into 1 cm × 1 cm stamps. Alexa Fluor 555-labeled FN solution, prepared by incubation of stock FN solution with 10× Alexa Fluor 555 NHS ester (10:1) for 1 h at room temperature (RT), was loaded on the pattern side of a PDMS stamp (5 µl, working concentration 100 µg/ml in PBS) for 30 min at RT. To spread the solution on the stamp, a glass coverslip was placed on the FN solution. After 30 min, the FN solution was removed and the PDMS stamp was sequentially washed with deionized water. The compressed air–dried PDMS stamp was placed on a flat precleaned PDMS stamp (5 min in UVO-Cleaner Model 18, Jelight Company), and a weight of 25 g was applied for 1 min. Subsequent surface passivation was done by incubation with a 2% water solution of Pluronic F127 (P2443, Sigma) in PBS (10010-031, Gibco) for 30 min. Homogeneous coating of precleaned micropillars/microgrooves/flat PDMS surfaces and glass substrates was done with 10 µg/ml of fibronectin PBS solution overnight at 4°C.

Cell cultures and cell culture reagents

For all experiments, wt MEF, MEF 2B–/–, and COS-7 cells were maintained in DMEM (11965-092, Gibco) containing 5% FBS (16000-044, Gibco). Trypsin-EDTA 0.05% (25300-054, Gibco) was used to detach cells. Blebbistatin (ab120425, Abcam), Y-23732 (ab120129, Abcam), and nocodazole (M1404, Sigma) were used as indicated. All plasmids were acquired from Addgene: CLIP170-mEmerald (#54044), NM2A-BFP2 (#55315), NM2A-mEmerald (#54190), NM2B-mEmerald (#54192), LifeAct-mOrange2 (#88840). Transfections were performed in Opti-MEM (31985-070, Gibco) using SuperFect reagent (301307, Qiagen) according to the manufacturer's protocol.

Antibodies and dyes

Antibodies were α-tubulin (ab18251, Abcam), detyrosinated α-tubulin (ab43389, Abcam), β-tubulin (T7816, Sigma), β-actin (A5441, Sigma), NM2A (909801, BioLegend), NM2B (909901, BioLegend), Alexa Fluor 568 goat anti-mouse (A-11004, ThermoFisher Scientific), Alexa Fluor 568 goat anti-rabbit (A-11011, ThermoFisher Scientific), Alexa Fluor 488 goat anti-mouse (A32723, ThermoFisher Scientific), Alexa Fluor 488 goat anti-rabbit (A-11034, ThermoFisher Scientific). Phalloidin (ab176753, Abcam), DAPI (D3571, Invitrogen), and Alexa Fluor 555 NHS ester (A37571, ThermoFisher Scientific).

Immunocytochemistry, immunoblot, and capillary-based immunoassay

Cell samples were fixed and permeabilized with 4% paraformaldehyde (158127, Sigma-Aldrich) and 0.05% Triton X-100 (T8787, Sigma-Aldrich) in PBS for 15 min at RT or with methanol (322415, Sigma-Aldrich) for 10 min at –20°C. Samples were washed three times with 10% nonfat dry milk (Nestle) in PBS. To block nonspecific binding, samples were treated with 10% milk in PBS for 1 h at RT and subsequently stained with a 1:500 dilution of primary antibodies in 10% milk in PBS overnight at 4°C, washed three times (5 min) with 10% milk in PBS, additionally stained with 1:500 secondary antibodies and 1:5000 DAPI in 10% nonfat dry milk in PBS for 2 h at RT, and then washed three times (5 min) with PBS. The stained samples were mounted in glass-bottomed dishes (P35G-1.5-20-C, MatTek) using ProLong Diamond Antifade (P36961, Invitrogen).

Immunoblots were carried out as described previously (Ma *et al.*, 2007). NM2A capillary-based immunoassays were done by Collaborative Protein Technology Resource (National Cancer Institute) according to the manufacturer's protocol (Peggy Sue system, ProteinSimple).

Data acquisition and analysis

Phase contrast microscopy was carried out using an inverted Olympus IX70 microscope. Confocal microscopy and FRAP experiments were performed using a Zeiss 880 microscope. Instant structural illumination microscopy (iSIM) was performed using a custom-built iSIM microscope (Visitech Intl.).

Immunoblot densitometry was performed using FIJI software, v.1.52d. Analysis of cell protrusions was performed manually. Cell directionality was analyzed using the Directionality plugin (FIJI). Cell aspect ratio measurements were computed by fitting ellipses (FIJI). Cell motility was analyzed with the Manual Tracking plugin (FIJI). NM2A and phalloidin occupancy of cell projection area was computed by the Freehand tool (FIJI) and Threshold Analyze particles plugins (FIJI) for "Max Intensity" projection images (Z Project, FIJI). Whole-cell heights were derived from iSIM *z*-stacks (FIJI). Three-dimensional reconstructions were done with the 3D Viewer plugin (FIJI). Analysis of microtubule alignment was performed by the Directionality plugin (FIJI) for microtubules within a single focal plane at the cell–surface interface (for images with normalized intensity).

Angular divergence was measured using the Angle tool (FIJI). FRAP data analysis was carried out using easyFRAP software (https://easyfrap.vmnet.upatras.gr/).

Data are presented as mean ± standard deviation. All statistical tests were done in Excel 365. *p* values were calculated for two-sample unequal-variance two-tailed *t* tests with the exception of *p* values calculated for Kolmogorov–Smirnov tests and Pearson statistics. Histograms and plots were made using Excel 365.

ACKNOWLEDGMENTS

This work was enhanced by advice from Sachiyo Kawamoto and Mary Anne Conti (National Heart, Lung, and Blood Institute [NHLBI]); Tatyana Svitkina (University of Pennsylvania); Bridgette Heine, Kem A. Sochacki, and Justin W. Taraska (NHLBI); and Christian Combs and Daniela Malide (NHLBI). It was supported by the NHLBI Division of Intramural Research (HL006209), a Research Scholar Grant, RSG-14-171-01-CSM, from the American Cancer Society to P.P.P., and the National Institutes of Health (R01CA181385 and U54CA210190 University of Minnesota Physical Sciences in Oncology Center to P.P.P.).

REFERENCES

Bao J, Jana SS, Adelstein RS (2005). Vertebrate nonmuscle myosin II isoforms rescue small interfering RNA-induced defects in COS-7 cell cytokinesis. J Biol Chem 280, 19594–19599.

Beach JR, Shao L, Remmert K, Li D, Betzig E, Hammer, John A III (2014). Nonmuscle myosin II isoforms coassemble in living cells. Curr Biol 24, 1160–1166.

Bouchet BP, Akhmanova A (2017). Microtubules in 3D cell motility. J Cell Sci 130, 39–50.

Brabletz T, Kalluri R, Nieto MA, Weinberg RA (2018). EMT in cancer. Nat Rev Cancer 18, 128.

Brown JA, Wysolmerski RB, Bridgman PC (2009). Dorsal root ganglion neurons react to semaphorin 3A application through a biphasic response that requires multiple myosin II isoforms. Mol Biol Cell 20, 1167–1179.

Burnette DT, Shao L, Ott C, Pasapera AM, Fischer RS, Baird MA, Der Loughian C, Delanoe-Ayari H, Paszek MJ, Davidson MW, *et al.* (2014). A contractile and counterbalancing adhesion system controls the 3D shape of crawling cells. J Cell Biol 205, 83–96.

Colin A, Singaravelu P, Thery M, Blanchoin L, Gueroui Z (2018). Actin-network architecture regulates microtubule dynamics. Curr Biol 28, 2647–2656.e2644.

Dogterom M, Koenderink GH (2019). Actin–microtubule crosstalk in cell biology. Nat Rev Mol Cell Biol 20, 38–54.

Doyle AD, Wang FW, Matsumoto K, Yamada KM (2009). One-dimensional topography underlies three-dimensional fibrillar cell migration. J Cell Biol 184, 481–490.

Erdogan B, Ao M, White LM, Means AL, Brewer BM, Yang L, Washington MK, Shi C, Franco OE, Weaver AM, *et al.* (2017). Cancer-associated fibroblasts promote directional cancer cell migration by aligning fibronectin. J Cell Biol 216, 3799–3816.

Even-Ram S, Doyle AD, Conti MA, Matsumoto K, Adelstein RS, Yamada KM (2007). Myosin IIA regulates cell motility and actomyosin-microtubule crosstalk. Nat Cell Biol 9, 299–309.

Gurtner GC, Werner S, Barrandon Y, Longaker MT (2008). Wound repair and regeneration. Nature 453, 314.

Harrison RG (1912). The cultivation of tissues in extraneous media as a method of morpho-genetic study. Anat Rec 6, 181–193.

Hay ED (2005). The mesenchymal cell, its role in the embryo, and the remarkable signaling mechanisms that create it. Dev Dyn 233, 706–720.

Heck JN, Ponik SM, Garcia-Mendoza MG, Pehlke CA, Inman DR, Eliceiri KW, Keely PJ (2012). Microtubules regulate GEF-H1 in response to extracellular matrix stiffness. Mol Biol Cell 23, 2583–2592.

Hung W-C, Yang JR, Yankaskas CL, Wong BS, Wu P-H, Pardo-Pastor C, Serra SA, Chiang M-J, Gu Z, Wirtz D, *et al.* (2016). Confinement sensing and signal optimization via Piezo1/PKA and myosin II pathways. Cell Rep 15, 1430–1441.

Jana SS, Kim K-Y, Mao J, Kawamoto S, Sellers JR, Adelstein RS (2009). An alternatively spliced isoform of non-muscle myosin II-C is not regulated by myosin light chain phosphorylation. J Biol Chem 284, 11563–11571.

Jansen KA, Donato DM, Balcioglu HE, Schmidt T, Danen EHJ, Koenderink GH (2015). A guide to mechanobiology: where biology and physics meet. Biochim Biophys Acta 1853, 3043–3052.

Janson ME, de Dood ME, Dogterom M (2003). Dynamic instability of microtubules is regulated by force. J Cell Biol 161, 1029–1034.

Kassianidou E, Hughes JH, Kumar S (2017). Activation of ROCK and MLCK tunes regional stress fiber formation and mechanics via preferential myosin light chain phosphorylation. Mol Biol Cell 28, 3832–3843.

Kassianidou E, Kumar S (2015). A biomechanical perspective on stress fiber structure and function. Biochim Biophys Acta 1853, 3065–3074.

Kassianidou E, Probst D, Jäger J, Lee S, Roguet A-L, Schwarz US, Kumar S (2019). Extracellular matrix geometry and initial adhesive position determine stress fiber network organization during cell spreading. Cell Rep 27, 1897–1909.e1894.

Kovács M, Thirumurugan K, Knight PJ, Sellers JR (2007). Load-dependent mechanism of nonmuscle myosin 2. Proc Natl Acad Sci USA 104, 9994–9999.

Kovács M, Wang F, Hu A, Zhang Y, Sellers JR (2003). Functional divergence of human cytoplasmic myosin II: kinetic characterization of the non-muscle IIA isoform. J Biol Chem 278, 38132–38140.

Lee K, Kim EH, Oh N, Tuan NA, Bae NH, Lee SJ, Lee KG, Eom CY, Yim EK, Park S (2016). Contribution of actin filaments and microtubules to cell elongation and alignment depends on the grating depth of microgratings. J Nanobiotechnol 14, 35.

Li Y, Lalwani AK, Mhatre AN (2008). Alternative splice variants of MYH9. DNA Cell Biol 27, 117–125.

Li Y, Lovett D, Zhang Q, Neelam S, Kuchibhotla RA, Zhu R, Gundersen GG, Lele TP, Dickinson RB (2015). Moving cell boundaries drive nuclear shaping during cell spreading. Biophys J 109, 670–686.

Lo CM, Buxton DB, Chua GC, Dembo M, Adelstein RS, Wang YL (2004). Nonmuscle myosin IIb is involved in the guidance of fibroblast migration. Mol Biol Cell 15, 982–989.

Loesberg WA, te Riet J, van Delft FCMJM, Schön P, Figdor CG, Speller S, van Loon JJWA, Walboomers XF, Jansen JA (2007). The threshold at which substrate nanogroove dimensions may influence fibroblast alignment and adhesion. Biomaterials 28, 3944–3951.

Lomakin AJ, Lee KC, Han SJ, Bui DA, Davidson M, Mogilner A, Danuser G (2015). Competition for actin between two distinct F-actin networks defines a bistable switch for cell polarization. Nat Cell Biol 17, 1435–1445.

Ma X, Bao J, Adelstein RS (2007). Loss of cell adhesion causes hydrocephalus in nonmuscle myosin II-B–ablated and mutated mice. Mol Biol Cell 18, 2305–2312.

Missirlis D, Haraszti T, Scheele CVC, Wiegand T, Diaz C, Neubauer S, Rechenmacher F, Kessler H, Spatz JP (2016). Substrate engagement of integrins $\alpha_5\beta_1$ and $\alpha_v\beta_3$ is necessary, but not sufficient, for high directional persistence in migration on fibronectin. Sci Rep 6, 23258.

Mogilner A, Keren K (2009). The shape of motile cells. Curr Biol 19, R762–R771.

Nalbant P, Chang Y-C, Birkenfeld J, Chang Z-F, Bokoch GM (2009). Guanine nucleotide exchange factor-H1 regulates cell migration via localized activation of RhoA at the leading edge. Mol Biol Cell 20, 4070–4082.

Nesmith AP, Grosberg A, Seywerd JN, Alford PW, Parker KK (2011). Vascular smooth muscle contractility depends on cell shape. Integr Biol 3, 1063–1070.

Oakley C, Brunette DM (1995). Topographic compensation: guidance and directed locomotion of fibroblasts on grooved micromachined substrata in the absence of microtubules. Cell Motil Cytoskeleton 31, 45–58.

Pegtel DM, Ellenbroek SI, Mertens AE, van der Kammen RA, de Rooij J, Collard JG (2007). The Par–Tiam1 complex controls persistent migration by stabilizing microtubule-dependent front–rear polarity. Curr Biol 17, 1623–1634.

Pellegrin S, Mellor H (2007). Actin stress fibres. J Cell Sci 120, 3491.

Preciado Lopez M, Huber F, Grigoriev I, Steinmetz MO, Akhmanova A, Koenderink GH, Dogterom M (2014). Actin–microtubule coordination at growing microtubule ends. Nat Commun 5, 4778.

Provenzano PP, Inman DR, Eliceiri KW, Trier SM, Keely PJ (2008). Contact guidance mediated three-dimensional cell migration is regulated by Rho/ROCK-dependent matrix reorganization. Biophys J 95, 5374–5384.

Sandquist JC, Swenson KI, Demali KA, Burridge K, Means AR (2006). Rho kinase differentially regulates phosphorylation of nonmuscle myosin II isoforms A and B during cell rounding and migration. J Biol Chem 281, 35873–35883.

Schiffhauer ES, Luo T, Mohan K, Srivastava V, Qian X, Griffis ER, Iglesias PA, Robinson DN (2016). Mechanoaccumulative elements of the mammalian actin cytoskeleton. Curr Biol 26, 1473–1479.

Schiffhauer ES, Ren Y, Iglesias VA, Kothari P, Iglesias PA, Robinson DN (2019). Myosin IIB assembly state determines its mechanosensitive dynamics. J Cell Biol 218, 895.
Shutova MS, Asokan SB, Talwar S, Assoian RK, Bear JE, Svitkina TM (2017). Self-sorting of nonmuscle myosins IIA and IIB polarizes the cytoskeleton and modulates cell motility. J Cell Biol 216, 2877.
Siegrist SE, Doe CQ (2007). Microtubule-induced cortical cell polarity. Genes Dev 21, 483–496.
Solinet S, Mahmud K, Stewman SF, Ben El Kadhi K, Decelle B, Talje L, Ma A, Kwok BH, Carreno S (2013). The actin-binding ERM protein moesin binds to and stabilizes microtubules at the cell cortex. J Cell Biol 202, 251–260.
Suter DM, Miller KE (2011). The emerging role of forces in axonal elongation. Prog Neurobiol 94, 91–101.
Tabdanov ED, Puram V, Zhovmer A, Provenzano PP (2018). Microtubule–actomyosin mechanical cooperation during contact guidance sensing. Cell Rep 25, 328–338.e325.
Tortosa E, Adolfs Y, Fukata M, Pasterkamp RJ, Kapitein LC, Hoogenraad CC (2017). Dynamic palmitoylation targets MAP6 to the axon to promote microtubule stabilization during neuronal polarization. Neuron 94, 809–825.e807.
Turney SG, Bridgman PC (2005). Laminin stimulates and guides axonal outgrowth via growth cone myosin II activity. Nat Neurosci 8, 717–719.
Vasiliev JM, Gelfand IM, Domnina LV, Ivanova OY, Komm SG, Olshevskaja LV (1970). Effect of colcemid on the locomotory behaviour of fibroblasts. J Embryol Exp Morphol 24, 625–640.
Vassilev V, Platek A, Hiver S, Enomoto H, Takeichi M (2017). Catenins steer cell migration via stabilization of front–rear polarity. Dev Cell 43, 463–479.e465.
Vicente-Manzanares M, Ma X, Adelstein RS, Horwitz AR (2009). Non-muscle myosin II takes centre stage in cell adhesion and migration. Nat Rev Mol Cell Biol 10, 778–790.
Vishavkarma R, Raghavan S, Kuyyamudi C, Majumder A, Dhawan J, Pullarkat PA (2014). Role of actin filaments in correlating nuclear shape and cell spreading. PLoS One 9, e107895.
Walboomers XF, Monaghan W, Curtis ASG, Jansen JA (1999). Attachment of fibroblasts on smooth and microgrooved polystyrene. J Biomed Mater Res 46, 212–220.
Wang F, Kovacs M, Hu A, Limouze J, Harvey EV, Sellers JR (2003). Kinetic mechanism of non-muscle myosin IIB: functional adaptations for tension generation and maintenance. J Biol Chem 278, 27439–27448.
Weiss P (1945). Experiments on cell and axon orientation in vitro: the role of colloidal exudates in tissue organization. J Exp Zool 100, 353–386.
Weiss P, Garber B (1952). Shape and movement of mesenchyme cells as functions of the physical structure of the medium: contributions to a quantitative morphology. Proc Natl Acad Sci USA 38, 264–280.
Williamson T, Gordon-Weeks PR, Schachner M, Taylor J (1996). Microtubule reorganization is obligatory for growth cone turning. Proc Natl Acad Sci USA 93, 15221–15226.